Size-resolved isotope analysis reveals anthropogenic reactive nitrogen transport and transformation in Taiwan mountain forests

Wen-Chien Lee,[1] Ming-Hao Huang,[1] Wei-Chieh Huang,[1] Jen-Ping Chen,[1] Yen-Jen Lai,[2,3] Haojia Ren,[4]* and Hui-Ming Hung[1]*

[1] Department of Atmospheric Sciences, National Taiwan University, Taipei, 10617, Taiwan

[2] Experimental Forest, National Taiwan University, Nantou, 557004, Taiwan

[3] Department of Agricultural Chemistry, National Taiwan University, Taipei, 10617, Taiwan

[4] Department of Geosciences, National Taiwan University, Taipei, 10617, Taiwan

Correspondence to: Haojia Ren (abbyren@ntu.edu.tw) and Hui-Ming Hung (hmhung@ntu.edu.tw)

Abstract.

Reactive nitrogen (Nr) species such as particulate ammonium ($p\mathrm{NH_4^+}$) and nitrate ($p\mathrm{NO_3^-}$) are critical drivers of air pollution and ecosystem health, yet their transformation processes in mountain forests are not well-characterized. We address this by combining size-segregated aerosol sampling at Xitou, Taiwan, with sensitive isotopic techniques and Bayesian modeling. Functional groups were analyzed by Fourier-transform infrared spectroscopy (FTIR-ATR), and isotopes $\delta^{15}\mathrm{N}$ and $\delta^{18}\mathrm{O}$ were measured by gas chromatography-isotope ratio mass spectrometry (GC-IRMS), enabling quantification of $p\mathrm{NH_4^+}$ source contributions and $p\mathrm{NO_3^-}$ formation pathways. Typical diurnal patterns, with higher daytime particle concentrations, were disrupted during a 26-hour fog with stagnant conditions, suppressing the advection of isotopically enriched urban plumes and promoting aqueous phase gas-particle isotopic re-equilibration. Under clear conditions, size-resolved $\delta^{15}\mathrm{N}$-$\mathrm{NH_4^+}$ exhibited a bell-shaped distribution peaking at the accumulation mode, but this gradient flattened during fog. Size-resolved $\delta^{15}\mathrm{N}$ and $\delta^{18}\mathrm{O}$ results of $p\mathrm{NO_3^-}$ revealed two distinct nitrate formation regimes: urban plumes retained $\mathrm{O_3}$-driven oxidation signatures with higher $\delta^{18}\mathrm{O}$, and rural/local regimes dominated by $\mathrm{RO_2}$-involved processes with greater isotopic depletion and enhanced biogenic contributions. Bayesian modeling indicated that 50−83% of $\mathrm{NH_3}$ emissions originated from combustion-related sources, while $\mathrm{RO_2}$-initiated oxidation dominated daytime $p\mathrm{NO_3^-}$ formation (42−95%) and heterogeneous reactions contributed 6−84% at night. These findings emphasize the importance of controlling urban $\mathrm{NO_x}$ and combustion-related $\mathrm{NH_3}$ emissions and demonstrate how size-resolved isotope analysis elucidates aerosol evolution along transport pathways.

1. Introduction

Anthropogenic activities have significantly altered the global reactive nitrogen (Nr) cycle, with profound implications for climate change, biodiversity loss, acid deposition, and air quality. Among Nr species, particulate ammonium ($p\mathrm{NH_4^+}$) and nitrate ($p\mathrm{NO_3^-}$) derived from ammonia ($\mathrm{NH_3}$) and nitrogen oxides ($\mathrm{NO_x}$), respectively, are major pollutants that degrade visibility and increase human morbidity (Gong et al., 2024; Zhang et al., 2017). In Asian regions, these species account for approximately 10−37% of non-refractory $\mathrm{PM_1}$ (particulate matter with a diameter less than 1 μm) mass (Zhou et al., 2020). While anthropogenic Nr is frequently transported to rural and remote areas, its distribution remains heterogeneous, exacerbating regional disparities in nitrogen deposition and

environmental impacts (Galloway et al., 2008). Therefore, understanding the formation pathways, transport mechanisms, and sources of Nr is essential for evaluating its origins and ecological impacts.

Nr is emitted from a diverse array of anthropogenic and biogenic sources. NH_3 is predominantly released from agricultural activities and is removed through dry deposition, precipitation scavenging, and chemical conversion to $p\mathrm{NH_4^+}$ via reactions with acidic precursors from NO_x and sulfur dioxide (SO_2) oxidations (Meng et al., 2017). Sources of NO_x include coal combustion, vehicle exhausts, biomass burning, and soil emissions (Fan et al., 2020). In the presence of sunlight, NO_x undergoes rapid oxidation through ozone (O_3) or peroxy radical (RO_2) pathways (termed P_{O_3} and P_{RO_2}, respectively) before converting to nitric acid (HNO_3) via the following reactions:

$$\mathrm{NO + O_3\,(or\ RO_2) \rightarrow NO_2 + O_2\,(or\ RO)} \quad \text{(R1)}$$

$$\mathrm{NO_2 + } h\nu \xrightarrow{\mathrm{O_2}} \mathrm{NO + O_3} \quad \text{(R2)}$$

$$\mathrm{NO_2 + OH + } M \rightarrow \mathrm{HNO_3} + M \quad \text{(R3)}$$

Tropospheric O_3 is a key oxidant formed from the photolysis of NO_2 (Haagen-Smit et al., 1953). Another important oxidant is the RO_2 radical, which is primarily formed through the reaction of VOC with hydroxyl radicals (OH) and might be more abundant in forested environments (Romer et al., 2016). Under nocturnal or low-light conditions, NO_x accumulates as nitrogen dioxide (NO_2) through reaction with O_3, which then undergoes heterogeneous reactions (termed as het) to produce HNO_3 as follows:

$$\mathrm{NO_2 + O_3 \rightarrow NO_3 + O_2} \quad \text{(R4)}$$

$$\mathrm{NO_3 + NO_2 + } M \rightarrow \mathrm{N_2O_5} + M \quad \text{(R5)}$$

$$\mathrm{N_2O_5 + H_2O_{(surface)} \rightarrow 2HNO_{3(}}_{aq\mathrm{)}} \quad \text{(R6)}$$

These oxidation processes leave distinct isotopic signatures for nitrate, making stable isotope analysis a robust tool for tracing the evolution of aerosol particles (Moore, 1977). Nitrogen isotope ratios ($\delta^{15}\mathrm{N} = [(^{15}R_{\mathrm{sample}})/(^{15}R_{\mathrm{air}}) - 1] \times 1000‰$, where ^{15}R is the ratio of $^{15}\mathrm{N}/^{14}\mathrm{N}$) are used to distinguish emission sources of $p\mathrm{NH_4^+}$ and transport of $p\mathrm{NO_3^-}$ (Savard et al., 2017; Chang et al., 2018), while oxygen isotope ratios ($\delta^{18}\mathrm{O} = [(^{18}R_{\mathrm{sample}})/(^{18}R_{\mathrm{VSMOW}}) - 1] \times 1000‰$, where ^{18}R is the ratio of $^{18}\mathrm{O}/^{16}\mathrm{O}$) in $p\mathrm{NO_3^-}$ provide insights into specific oxidation pathways, as each oxidant (O_3, OH, RO_2) imparts a unique isotopic fingerprint (Walters and Michalski, 2016). Although isotopic Bayesian mixing model frameworks (e.g., IsoSource, SIAR, or MixSIAR) have successfully identified the sources of Nr and the formation mechanisms of $p\mathrm{NO_3^-}$ (Fan et al., 2020; Chang et al., 2018; Kawashima et al., 2023; Pan et al., 2016), these processes are highly variable in complex terrains. Little is known about the sources and atmospheric processing of Nr in East Asian mountain forests, where local emissions and transported pollutants interact under high-humidity conditions (Guha et al., 2017). During transport, $\delta^{15}\mathrm{N}$ values are modified by kinetic fractionation and gas-particle partitioning, often leading to a progressive depletion of heavier isotopes (Gobel et al., 2013; Walters and Michalski, 2016). Furthermore, the typically low concentrations of mountain aerosols have historically limited detailed size-segregated isotopic analyses, constraining our understanding of emission sources and size-dependent nitrogen transformation pathways (Morin et al., 2009).

Xitou, a representative cloud forest in central Taiwan, serves as an ideal natural laboratory to address these gaps. Situated in a valley oriented toward urban regions, the site experiences predictable valley-mountain breeze circulations that transport anthropogenic plumes into a biogenic-rich environment where Nr accounts for 13–23% of PM_{10} mass (Chen et al., 2021). This mixing vessel is characterized by frequent fog and persistent humidity, with a mean relative humidity (RH) above 80%. Fog droplets serve as a reactive aqueous medium, facilitating the dissolution of Nr species and accelerating secondary aerosol formation through aqueous-phase oxidation, thereby modifying aerosol hygroscopicity and chemical aging (Ervens, 2015). Specifically, aqueous-phase nitrate formation

during fog proceeds via oxidation of NO_2 by ·OH radicals and heterogeneous hydrolysis of N_2O_5 on fog droplet surfaces. Furthermore, NO_2 disproportionation represents an additional pathway, a process enhanced by the larger radii of fog droplets compared to aerosol particles (Zhang et al., 2022; Lin et al., 2026; Yu et al., 2023). In addition, recent field research has demonstrated efficient nitrate formation during fog occurs mainly on fog interstitial aerosols through NO_2 and N_2O_5 hydrolysis, highlighting the importance of size-resolved characterization of aerosols under fog conditions (Xu et al., 2024).

While previous work at Xitou characterized winter Nr sources (Chen, T. Y. et al., 2022), the influence of prolonged fog and stagnant atmospheric conditions on isotopic distributions remains poorly resolved. In this study, we investigate the size-dependent isotope distribution of aerosols during a rare ~26-hour fog episode to examine how extreme humidity and suppressed transport modulate the transformation of pNH_4^+ and pNO_3^-. By combining size-segregated sampling with Bayesian source apportionment, we evaluate the relative contributions of local versus transported sources and evaluate how fog conditions affect the isotopic composition of Nr species in a subtropical mountain forest. This study provides valuable insights into aqueous-phase nitrogen processing, offering a clearer picture of how stagnant meteorological regimes alter chemical evolution in a subtropical mountain environment.

2. Methods

2.1. Site description and sampling

Field measurements were conducted from 17 to 24 April 2021 at the Xitou Experimental Forest of National Taiwan University (23°40'12" N, 120°47'54" E, 1179 m a.s.l.; Fig. S1). April represents the spring transition in Taiwan, a period characterized by frequent fog at Xitou, and a shift in aerosol loading from wintertime maxima to summertime minima. Size-segregated aerosol samples were collected during alternating daytime (09:00 to 17:00 LT, denoted as 'D') and nighttime (18:00 to 06:00 LT on the following day, denoted as 'N') intervals using a micro-orifice uniform deposit impactor (MOUDI, Model 125R, MSP Corporation, Shoreview, Minnesota, USA). The MOUDI was operated at a flow rate of 30 L min^{-1}, with aerodynamic cut-point diameters of 0.056, 0.1, 0.18, 0.32, 0.56, 1.0, 1.8, 3.2, 5.6, and 10 μm. The higher flow rate (30 vs. 10 L min^{-1}) relative to the prior winter study yielded greater particle mass for analysis. Sampling was conducted on 46.2 mm polytetrafluoroethylene (PTFE) filters (Whatman 7592-104) labeled by day and night intervals (e.g., "17D"). Samples were sealed in aluminum foil and stored at 4°C prior to analysis.

Meteorological parameters, including pressure, temperature, RH, trace gases, visibility, and radiation, were monitored by a custom-built Air Quality Box (AQB) and the on-site Agricultural Meteorological Station. Among the trace gases measured by AQB, carbon monoxide (CO) was selected as the primary tracer for analysis due to its reliable calibration (Huang, W. C. et al., 2024).

2.2. Sample analysis and isotope measurements

The analytical workflow involved: concentration screening, aqueous extraction, and isotopic measurements (Fig. 1). Initially, attenuated total reflectance Fourier transform infrared spectroscopy (ATR-FTIR, Nicolet 6700, Thermo Fisher Scientific, Madison, WI, USA) was used to semi-quantitatively screen filters for sufficient nitrogen content (≥ 1 μM N as $NO_3^- + NH_4^+$, with details in Supplementary Description S1). Filters from adjacent size bins with insufficient loading were combined, and a mass-weighted diameter was calculated as detailed in Supplementary Description S2.

Filters were extracted in 30 mL Milli-Q water (18.2 MΩ at 25°C) using 30-min ultrasonication, followed by filtering through 0.22 μm Millipore syringe filters. Total nitrogen (TN) was determined by oxidizing part of the extracts to nitrate (NO_3^-) using potassium persulfate. The bacterial denitrifier method was subsequently employed to measure the $\delta^{15}N$ of TN, and the $\delta^{15}N$ and $\delta^{18}O$ of nitrate + nitrite ($NO_3^- + NO_2^-$, NN). Two bacterial strains were employed: *Pseudomonas chlororaphis* (ATCC® 43928™, Manassas, VA, USA) for TN analysis and *Pseudomonas chlororaphis ssp. aureofaciens* (ATCC® 13985™, Manassas, VA, USA) for NN analysis to convert NO_3^- to nitrous oxide (N_2O) gas while preserving isotopic integrity (Weigand et al., 2016). Isotopic ratios of N_2O were measured via

gas chromatography-isotope ratio mass spectrometry (GC-IRMS) and calibrated against international isotope standards: USGS 34 ($\delta^{15}N = -1.8‰$; $\delta^{18}O = -27.93‰$) and IAEA-NO_3 ($\delta^{15}N = +4.7‰$; $\delta^{18}O = +25.61‰$) (Böhlke et al., 2003). Detailed descriptions of isotope measurement procedures are provided by Chen, T. Y. et al. (2022).

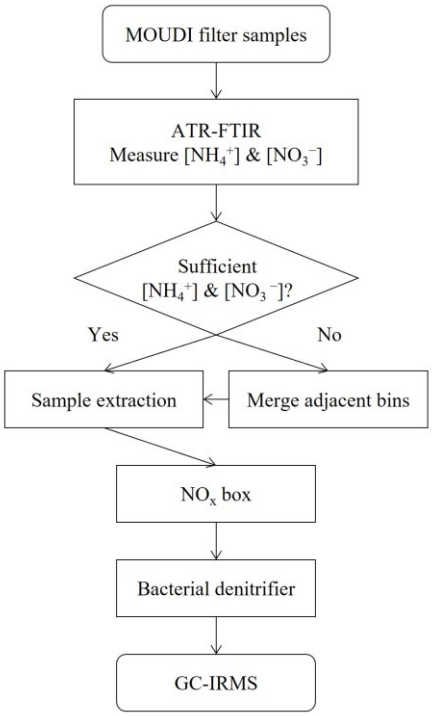

Figure 1. Schematic diagram of sampling and isotope analysis procedures.

Given that NO_2^- concentrations detected by IC analysis were negligible, NN values were considered as representative of pNO_3^- (i.e., $\delta^{15}N\text{-}NN \approx \delta^{15}N\text{-}NO_3^-$; $\delta^{18}O\text{-}NN \approx \delta^{18}O\text{-}NO_3^-$). If TN primarily comprises NH_4^+ and NN, the $\delta^{15}N$ of pNH_4^+ can be calculated via mass balance:

$$\delta^{15}\text{N-NH}_4^+ = \frac{\delta^{15}\text{N}_{\text{TN}} \times M_{\text{TN}} - \delta^{15}\text{N}_{\text{NN}} \times M_{\text{NN}}}{M_{\text{TN}} - M_{\text{NN}}} \quad (1)$$

where M_{TN} and M_{NN} represent the molarities of TN and NN, respectively, measured by the photolytic $NO/NO_2/NO_x$ analyzer (NO_x box, Model T200P, Teledyne API). Stringent quality control was applied: data points were excluded if NN exceeded 80% of TN or if NH_4^+ was less than 60% of water-soluble reduced nitrogen (i.e., $M_{TN}-M_{NN}$). The latter criterion was based on the assumption that contributions from organic nitrogen were negligible under these conditions. The NH_4^+ concentration was determined on a fluorescence spectrophotometer (Hitachi F-2700) using a fluorometric method (Holmes et al., 1999).

2.3. Bayesian isotope mixing model framework (MixSIAR)

Source contributions of NH_3 and the formation pathways of pNO_3^- were estimated using the MixSIAR framework (v3.1.12), which employs Bayesian models to estimate source contributions while accounting for uncertainties in source values (Stock et al., 2018). The model follows the general form as follows:

$$X_{ij} = \sum_{k=1}^{n} P_k \times S_{jk} + err_{ij} \quad (2)$$

where X_{ij} is the measured isotope value of tracer j (δ^{15}N-NH_4^+ or δ^{18}O-NO_3^-) for sample i, P_k is the proportion of source k with $\sum P_k = 1$, S_{jk} is the isotope value of source k (as a normal distribution with mean values and standard deviations), and err_{ij} is the residual error. The model was run with extended Markov Chain Monte Carlo (MCMC) parameters to ensure convergence, with all runs confirmed to have converged based on the Gelman-Rubin potential scale reduction factor and the Geweke diagnostic (Stock and Semmens, 2016). Results are reported as mean source contributions with associated standard deviations. To further assess model performance, reconstructed X_{ij} was calculated by weighting S_{jk} with the model-derived P_k and compared to the measured X_{ij}.

2.3.1. Source apportionments of NH_3

To account for isotopic fractionation during the NH_3 to pNH_4^+ transition, the initial δ^{15}N-NH_3 (i.e., δ^{15}N-NH_3^0) was estimated from the concentration-weighted mean δ^{15}N-NH_4^+ following Pan et al. (2016):

$$\delta^{15}\text{N-NH}_3^{\,0} = \delta^{15}\text{N-NH}_4^+ - \varepsilon_{\text{NH}_4^+-\text{NH}_3}\left(1-f\right), \tag{3}$$

where $\varepsilon_{\text{NH}_4^+-\text{NH}_3}$ is the isotope fractionation constant (+33‰ for equilibrium isotope effect (EIE) between $NH_{3(g)}$ and $pNH_4^+{}_{(aq/s)}$) (Heaton et al., 1997), and f is the fraction of pNH_4^+ in the NH_3–pNH_4^+ system. Sensitivity tests regarding the temperature dependence, gas–particle equilibrium, and the approximation of equilibrium on $\varepsilon_{\text{NH}_4^+-\text{NH}_3}$ were performed, as detailed in Supplementary Description S3 and Table S1 (Chang et al., 2025). The f values were derived from the Community Multiscale Air Quality (CMAQ) model (version 4.7.1), incorporating meteorological data from the Weather Research and Forecasting (WRF) model (version 3.7.1) and the emission database from the Taiwan Emission Data System (version 12) (Tsai et al., 2024). The model-simulated pNH_4^+ mass concentrations agreed with laboratory measurements within a 20% uncertainty range (Fig. S2).

For NH_3 source apportionment, four major emission sources were considered: fertilizer (−28.3±5.8‰), waste (−17.6±5.6‰), NH_3 slip (−8.2±5.5‰), and fossil fuel emissions (1.8±3.2‰) (Kawashima et al., 2023). These sources can be categorized into two groups based on their δ^{15}N-NH_3 signatures: (1) volatilization-related sources (fertilizer and waste) with lower δ^{15}N-NH_3 values, and (2) combustion-related sources (NH_3 slip and fossil fuel emissions) with higher values (Chen, Z.-L. et al., 2022). δ^{15}N-NH_3 obtained using passive techniques was adjusted by 15‰ to account for systematic differences between collection methods (Kawashima et al., 2023; Walters et al., 2020). Statistical values for MixSIAR analysis are provided in Table S2.

2.3.2. Estimating formation pathways of pNO_3^-

δ^{18}O-NO_3^- is applied to evaluate the relative contributions of various HNO_3 formation. Six potential pathways were considered by combining the primary oxidants (P_{O_3} and P_{RO_2}) with three terminal mechanisms (OH1, OH2, and heterogeneous processes (het)). These pathways are characterized by their specific δ^{18}O-NO_3^- signatures (Fig. S3), calculated using a mass-balance approach assuming no kinetic isotope fractionation (Walters and Michalski, 2016). RO_2 was assigned a δ^{18}O of 23.5‰, reflecting that O in RO_2 originates from molecular O_2 (Kroopnick and Craig, 1972). O_3 exhibits elevated δ^{18}O values ranging from 90 to 122‰ (Hastings et al., 2003). OH radicals were split into OH1 (−15 to 0‰) (Dubey et al., 1997), and OH2 (38 to 61‰). Daytime mechanisms included $P_{RO_2\text{-OH1}}$ (33–49‰), $P_{RO_2\text{-OH2}}$ (50–69‰), $P_{O_3\text{-OH1}}$ (55–81‰), and $P_{O_3\text{-OH2}}$ (73–102‰). Nighttime analysis focused on $P_{RO_2\text{-het}}$ (50–69‰) and $P_{O_3\text{-het}}$ (73–102‰), while retaining $P_{RO_2\text{-OH1}}$ to account for residual daytime nitrate that persists into the night. Sensitivity analyses regarding pathway exclusion are detailed in Supplementary Description S4, Tables S3 and S4.

3. Results and discussion

3.1. Environmental variabilities

Figure 2 shows the temporal evolution of key environmental parameters, including temperature (Temp), relative humidity (RH), wind speed (WS), wind direction (WD), radiation (Rad), visibility (Vis), and carbon monoxide (CO) concentration for the sampling period. During clear-sky periods, the site exhibited pronounced diurnal cycles driven by complex terrain. Daytime temperatures (20±2 °C) were consistently higher than nighttime values (15±1 °C). Conversely, RH peaked at night (99±1 %) and reached a minimum during daytime (87±8 %). Wind patterns followed typical valley-mountain circulation, with daytime valley winds predominant from the north (316°−33°) while nighttime mountain breezes shifted to the southeast (124°−179°), consistent with previous observations (Chen et al., 2021). This circulation, often coupled with sea breezes inland penetration, facilitated the diurnal upslope transport of air masses from low-altitude urban areas toward the mountain forest, likely introducing anthropogenic pollutants. This transport mechanism is further evidenced by CO concentrations, a reliable tracer of combustion emissions, which were consistently higher during the daytime (0.23±0.03 ppm) than at nighttime (0.14±0.03 ppm).

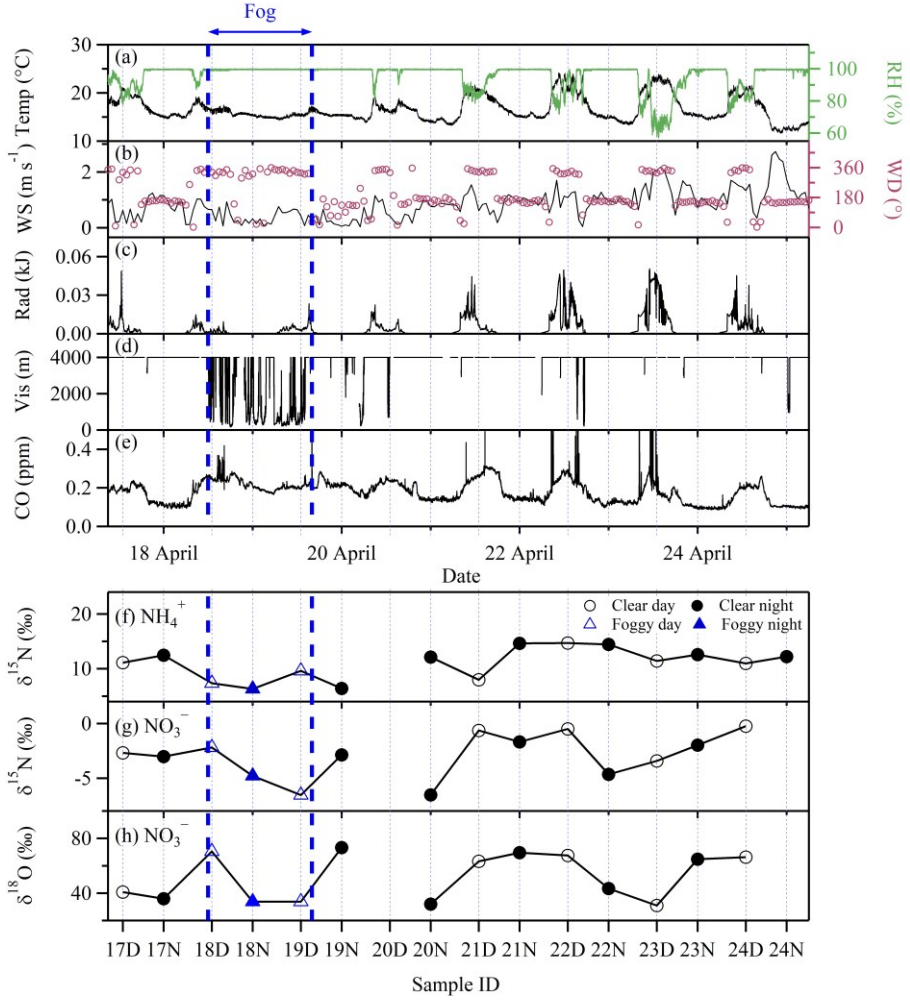

Figure 2. Time series of various environmental parameters measured from 17−24 April 2021, including (a) temperature (Temp) and relative humidity (RH), (b) wind speed (WS) and wind direction (WD), (c) radiation (Rad), (d) visibility (Vis), and (e) CO concentration. The concentration-weighted isotope values for (f) δ^{15}N-NH_4^+, (g) δ^{15}N-NO_3^-, and (h) δ^{18}O-NO_3^- over daytime (09:00−17:00 LT, D) and nighttime (18:00−06:00 LT the next day, N) sampling periods. Uncertainties for δ^{15}N and δ^{18}O measurements are generally less than 0.1‰ and are smaller than the symbol size.

A significant departure from these typical diurnal patterns occurred during a prolonged fog episode lasting approximately 26 hours (from 18 April 12:00 to 19 April 14:00). This event was characterized by visibility below 1000 m and RH exceeding 90% for at least one hour. During this episode, the local atmosphere became exceptionally stagnant: Mean wind speed decreased from 0.9±0.6 m s^{-1} to 0.5±0.5 m s^{-1}, with approximately 25% of observations < 0.1 m s^{-1}. Temperature (15±1 °C) and RH (99.5±0.2 %) remained relatively stable, effectively locking the meteorological state. Notably, CO concentrations during the foggy night (0.22±0.03 ppm) remained as high as clear-daytime levels. This lack of nocturnal ventilation suggests that pollutants were trapped within the valley, creating a quasi-closed system highly conducive to in-situ chemical transformations and aqueous-phase processing.

3.2. Size-resolved aerosol chemical composition

The impact of the prolonged fog on the mass concentration distributions of NH_4^+, NO_3^-, SO_4^{2-}, and black carbon (BC) as a function of particle size is shown in Fig. 3 (detailed temporal variation is provided in Fig. S4). Under the clear period (left panels), all four species exhibited higher daytime concentrations than nighttime values. NH_4^+, SO_4^{2-}, and BC peaked in the 0.32−0.56 μm range during the daytime, and shifted to 1−1.8 μm with a broader distribution and lower total concentrations at nighttime. In comparison, NO_3^- showed a bimodal distribution, with peaks at 0.56−1 μm and 3.2−5.6 μm during daytime, shifting to 1−1.8 μm and 3.2−5.6 μm at nighttime. These shifts likely reflect coagulation and hygroscopic growth under elevated nocturnal RH.

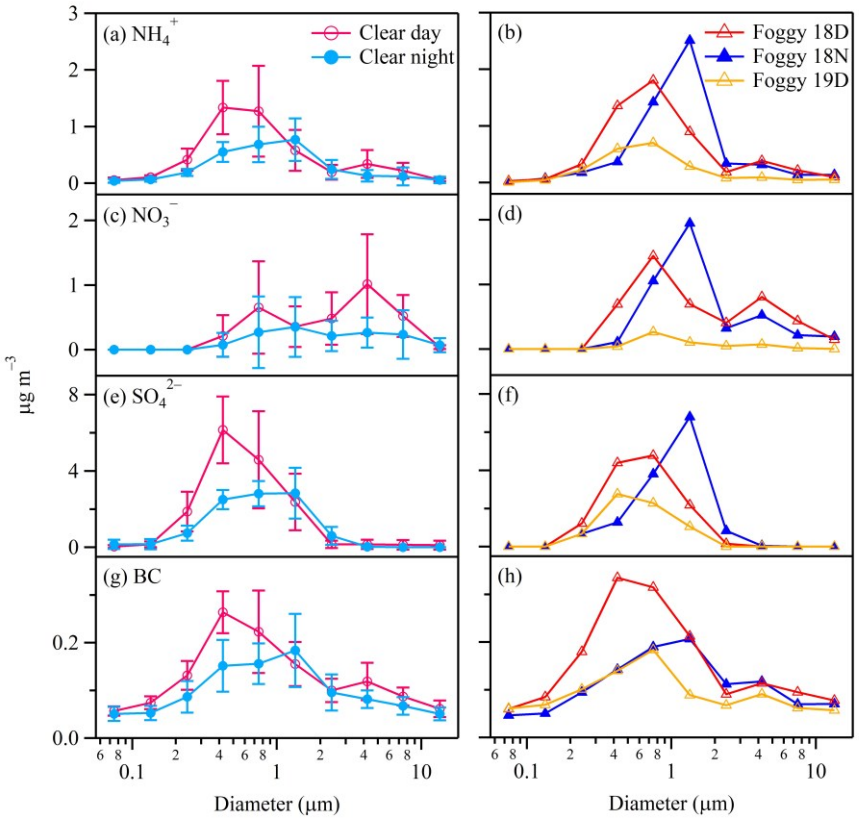

Figure 3. Size-resolved mass concentration distributions of particulate (a,b) NH_4^+, (c,d) NO_3^-, (e,f) SO_4^{2-}, and (g,h) black carbon (BC) estimated from FTIR analysis during clear (left panels) and foggy (right panels) periods.

During the foggy period (right panels), sub-micrometer NO_3^- concentrations increased on 18D, surpassing coarse-mode levels. This enhancement likely resulted from the accelerated HNO_3-NH_3 partitioning, promoted by the high surface-to-volume ratio and elevated water content of sub-micrometer particles during the onset of fog. By 18N, all species shift to the 1−1.8 μm range, indicating substantial hygroscopic growth and coagulation during the fog period. While total concentrations of NH_4^+, SO_4^{2-}, and NO_3^- remained relatively stable compared to 18D, the observed decrease in BC suggests a transition, where aqueous chemistry in the fog droplets compensated for the mass lost to deposition. In the subsequent interval (19D), concentrations of all species decreased, likely resulting from wet deposition of larger droplets and suppressed pollutant transport under stagnant conditions. These observations demonstrate that prolonged fog conditions not only enhance local chemical transformations but also fundamentally alter particle size distributions. Such shifts in composition and size provide the critical framework for interpreting isotopic fractionation and Nr transformations discussed in the following sections.

3.3. δ^{15}N-NH_4^+ and derivation of emitted δ^{15}N-NH_3

3.3.1. δ^{15}N-NH_4^+

The daily concentration-weighted δ^{15}N-NH_4^+ values at the Xitou site ranged from 6.31‰ to 14.69‰, with an average of 10.95 ± 2.76‰ (Fig. 2f, calculation details in Supplementary Description S5). These results are consistent with previous winter observations at this site (−3.7‰ to 21.39‰, with an average of 11.95 ± 2.65‰) (Chen, T. Y. et al., 2022). As shown in Fig. S5, these values fall between those typical of urban-influenced environments (19.6‰) and remote/forest sites (~5.6‰), reflecting the mixed-source characteristics of Xitou (Chen, T. Y. et al., 2022; Kawashima et al., 2023; Hall et al., 2016; Kundu et al., 2010; Moore, 1977; Proemse et al., 2012; Savard et al., 2017; Ti et al., 2018; Walters et al., 2022). The isotopic signature is particularly comparable to other semi-rural receptor sites in East Asia that receive diluted urban plumes mixed with regional agricultural background.

Temporal patterns showed higher δ^{15}N-NH_4^+ during the clear period, with daytime and nighttime averages of 11.22 ± 2.13‰ and 12.12 ± 2.53‰, respectively (Table 1). In contrast, lower values were observed during fog, including 7.35‰ (18D), 6.31‰ (18N), and 9.60‰ (19D). This decline of δ^{15}N during the fog likely results from three concurrent processes under stagnant conditions. First, stagnant conditions suppressed the transport of δ^{15}N-enriched urban plumes from nearby source regions. Second, continuous exchange between gas-phase NH_3 and pNH_4^+ shifts the particle phase toward the signature of the local NH_3 pool, which is depleted in δ^{15}N due to agricultural volatilization. Furthermore, wet deposition during fog may remove ^{15}N-enriched particles, forcing the remaining pNH_4^+ to re-equilibrate with an increasingly δ^{15}N-depleted gas phase. This observed decrease in δ^{15}N-NH_4^+ during the foggy period contrasts with our previous study, reporting slight increases during shorter fog events (< 6 hours) (Chen, T. Y. et al., 2022). The nearly double concentrations of both pNH_4^+ and pNO_3^- in this study than in those in Chen, T. Y. et al. (2022) might indicate a stronger partition of NH_3 into the particle phase, leading to much lower δ^{15}N-NH_4^+ in this study.

Table 1. Concentration-weighted isotope values (unit: ‰) under different weather circumstances.

	δ^{15}N-NH_4^+	δ^{15}N-NO_3^-	δ^{18}O-NO_3^-
All	10.81±2.72 (n = 15)	−2.98±1.97 (n = 14)	51.82±16.47 (n = 14)
Clear day	11.22±2.13 (n = 5)	−1.50±1.30 (n = 5)	53.74±14.99 (n = 5)
Clear night	12.12±2.53 (n = 7)	−3.46±1.67 (n = 6)	53.12±16.59 (n = 6)
Foggy 18D	7.35 (n = 1)	−2.19 (n = 1)	70.44 (n = 1)
Foggy 18N	6.31 (n = 1)	−4.80 (n = 1)	33.81 (n = 1)
Foggy 19D	9.60 (n = 1)	−6.54 (n = 1)	33.81 (n = 1)

Under clear conditions (excluding 19N and 21D), the size-resolved δ^{15}N-NH_4^+ distribution revealed a bell-shaped distribution (Fig. 4). Values peaked at ~15‰ in the accumulation mode (~0.5−2 μm) and decreased to ~7‰ in both the ultrafine and coarse particles. This pattern reflects a transition between local emissions and aged,

transported aerosols. For ultrafine mode (<0.5 μm), particles maintain isotopic equilibrium with the local NH_3 pool, dominated by δ^{15}N-depleted residual NH_3 or volatilization sources (typically −28.3‰ to −17.6‰). For accumulation-mode (~0.5–2 μm), particles preserve the signatures of lower-elevation anthropogenic emission regions. Here, combustion-derived NH_3 (typically −8.2‰ to 1.8‰) reacts with H_2SO_4 to form non-volatile ammonium sulfate and ammonium bisulfate. Unlike ammonium nitrate, which is more volatile and easily re-equilibrates with gas-phase NH_3 during transport, sulfate-bound NH_4^+ is more resistant to isotopic re-equilibration, allowing it to act as a conservative tracer of urban source signatures during upslope transport (Wu et al., 2022). For the coarse mode (> 2 μm), particles are likely dominated by mineral dust and sea salt and present a substantially weaker thermodynamic sink for NH_3 absorption compared to acidic fine-mode sulfate aerosols (Fig. S6) (Pye et al., 2020). Therefore, NH_4^+ in this mode likely maintains a dynamic equilibrium with local gas-phase NH_3, which becomes progressively depleted in ^{15}N as the air mass ages.

During fog, the bell-shaped distribution flattened significantly. Weakened wind suppressed the upslope transport of enriched anthropogenic pollutants, while enhanced aqueous-phase interaction promoted uniform isotopic re-equilibrium across all sizes. The high NO_3^- concentration from aqueous chemistry can also promote the local isotopically depleted NH_3 partitioning into the particle phase, dampening the size-dependent isotopic gradient.

The flat δ^{15}N-NH_4^+ size distribution was also observed on 19N and 21D. For 19N, it is likely a legacy effect of the preceding fog period (18D, 18N, and 19D). The NH_3 pool remained isotopically depleted from sustained fog-driven scavenging and re-equilibration, and regional transport had not yet replenished the accumulation-mode signal. However, high sub-micrometer NO_3^- concentration (Fig. S4) suggests that fog-like aqueous chemistry persisted, maintaining isotopic signatures similar to 18D. Conversely, the flat distribution on 21D reflects a distinct source influence. HYSPLIT back-trajectories (Fig. S7) indicate that the air parcel traveled through agricultural regions characterized by heavily depleted NH_3 (e.g., livestock waste, −28.3‰ to −17.6‰). The partitioning of this isotopically light NH_3 during transit effectively erased the characteristic accumulation-mode enrichment.

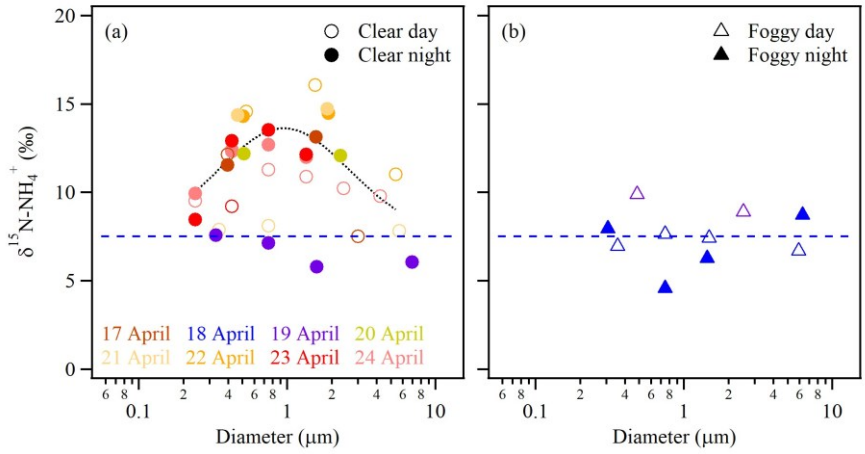

Figure 4. δ^{15}N of size-segregated pNH_4^+ during (a) clear and (b) foggy conditions. The dashed blue line indicates the mean δ^{15}N-NH_4^+ for foggy periods. The dotted curve represents LogNormal distribution fits for clear conditions, excluding 19N and 21D, where no distinct bell-shaped size dependence was identified.

3.3.2. δ^{15}N-NH_3^0 and source apportionment

The δ^{15}N-NH_3^0 values were derived using *f* values estimated from CMAQ-simulated NH_3 and measured pNH_4^+ concentrations (Fig. S8). The resulting δ^{15}N-NH_3^0 ranged from −12.55‰ to −6.71‰, consistently lower than the concentration-weighted δ^{15}N-NH_4^+, as shown in Fig. 5a. Based on the derived δ^{15}N-NH_3^0 values and assuming a single-source contribution, NH_3 can be mainly attributed to NH_3 slip. However, because real-world air parcels are

typically influenced by a complex mixture of emission sources, the MixSIAR Bayesian framework was employed to quantitatively assess multiple source contributions (Fig. 5b). Overall, combustion-related sources (fossil fuel and NH_3 slip) were the dominant contributors to NH_3^0 (i.e., $NH_4^+ + NH_3$) in the Xitou area, accounting for 50−83% of total NH_3 emissions. During periods with higher $\delta^{15}N\text{-}NH_3^0$, such as 17D, 17N, and 19D, fossil fuel combustion dominated (54±3%), followed by NH_3 slip (26±1%), waste (13±1%), and fertilizer (8±1%). In comparison, during periods with lower $\delta^{15}N\text{-}NH_3^0$, the source contributions were more evenly distributed. Fossil fuel combustion and NH_3 slip remain significant, accounting for 30±5% and 29±1%, respectively, while the relative contributions from waste and fertilizer sources increased to 24±2% and 17±3% (Fig. S9). Despite the sensitivity of $\varepsilon_{NH_4^+-NH_3}$ to temperature (Kawashima et al., 2023) and gas−particle equilibrium (Chang et al., 2025), the estimated $\delta^{15}N\text{-}NH_3^0$ consistently yielded MixSIAR results in which combustion-related sources accounted for 88–95% of total NH_3 emission (see Supplementary Description S3 and Table S1). The persistent dominance of combustion-related sources at this remote mountain site, even during the stagnant fog condition, demonstrates the influence of transport from urban and industrial areas. These findings underscore the need for regional emission control strategies targeting anthropogenic NH_3 sources, which may represent a more cost-effective mitigation strategy for Taiwan, potentially yielding greater air quality benefits than NO_x or SO_2 reductions alone (Huang, P. C. et al., 2024). It should be noted, however, that the differences in source contributions between daytime and nighttime periods, or between fog and clear conditions, remain within the overlapping ranges of the posterior distributions; consequently, the current sample number precludes statistically robust discrimination between these conditions. Expanded measurements encompassing multiple seasons and contrasting meteorological regimes would be necessary to establish whether systematic diurnal or fog-driven shifts in NH_3 source apportionment exist at this site.

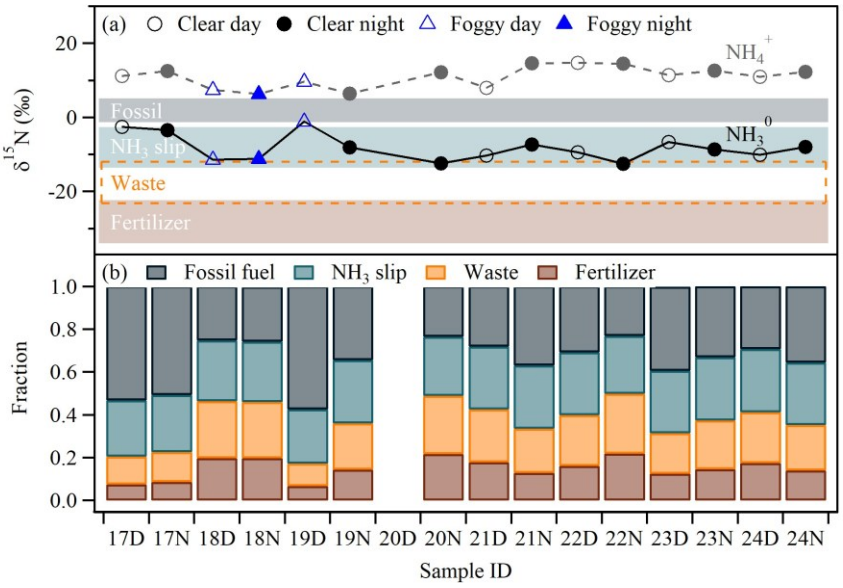

Figure 5. (a) Estimated $\delta^{15}N\text{-}NH_3^0$ at Xitou derived from measured $\delta^{15}N\text{-}NH_4^+$, and compared with the characteristic $\delta^{15}N$ ranges of NH_3 sources reported in the literature (Table S2). (b) Source apportionment results of NH_3 from the MixSIAR framework. Uncertainties of each contribution are shown in Fig. S9.

3.4. $\delta^{15}N$ and $\delta^{18}O$ of pNO_3^-

3.4.1. $\delta^{15}N\text{-}NO_3^-$

The daily concentration-weighted $\delta^{15}N\text{-}NO_3^-$ values ranged from −6.54‰ to −0.24‰, with an average of −2.98±1.97‰ (Fig. 2g). These values are consistent with those reported in mountain sites such as Mt. Lulin

(−3.6±3.8‰) (Guha et al., 2017) and the Himalayan-Tibetan Plateau (0.44±4.89‰) (Lin et al., 2021), as illustrated in Fig. S10. Compared to wintertime measurements at the same site (2.98±1.20‰) (Chen, T. Y. et al., 2022), these lower springtime values likely reflect seasonal shifts in NO_x sources and transport-related fractionation. The depletion relative to urban values, such as ~11.5‰ in Beijing and Gosan (Fan et al., 2020; Kundu et al., 2010), indicates that NO_x-to-HNO_3 conversion during transport to the mountain receptors is accompanied by progressive isotopic fractionation (Freyer et al., 1993; Gobel et al., 2013).

Under clear conditions, $\delta^{15}N\text{-}NO_3^-$ showed minor diurnal variation, with slightly higher values during daytime (−1.50±1.30‰) than nighttime (−3.46±1.67‰; Table 1), likely reflecting shifts between transported urban and local biogenic NO_x sources or the depletion through deposition. During the fog, $\delta^{15}N\text{-}NO_3^-$ decreased significantly from −2.19‰ (18D) to −4.80‰ (18N), and further to −6.54‰ (19D) (Fig. 2g). This decline, contrasting with previous shorter fog events (Chen, T. Y. et al., 2022), reflects the combined effects of prolonged stagnation and a reduced influx of urban air. These conditions promote enhanced aqueous-phase pNO_3^- formation, predominantly driven by $\delta^{15}N$-depleted NO_x from locally derived biogenic precursors or precursors that have undergone extensive fractionation during transport (Vicars et al., 2013; Gobel et al., 2013).

Relatively low concentration-weighted $\delta^{15}N\text{-}NO_3^-$ values observed outside the fog periods on 20N and 22N, likely attributable to distinct mechanisms. For 22N, the depletion is linked to enhanced local production, supported by elevated sub-micrometer NO_3^- concentration shown in Fig. S4. For 22N, the low $\delta^{15}N$ coincides with significant deposition loss, as evidenced by low total NO_3^- levels. Because HNO_3 readily reacts with coarse-mode mineral dust and sea salt, the deposition efficiency during transport is high; this preferential removal of $\delta^{15}N$-enriched species often leaves the residual nitrate pool isotopically lower. Furthermore, the thermodynamic partitioning of HNO_3, governed by ambient temperature and particle acidity regulated by sulfate and ammonium, critically influences the observed $\delta^{15}N$. Ultimately, the observed $\delta^{15}N$ at this site serves as an integrated signal of physical and chemical dynamics processes within the air parcel during its transit.

Size-segregated $\delta^{15}N\text{-}NO_3^-$ values ranged from −10.05 to 0.78‰, showing a weak positive correlation with particle diameter (Fig. 6a). Fine particles (PM_1) had slightly lower $\delta^{15}N\text{-}NO_3^-$ values (−3.59±2.38‰) compared to larger, coarse-mode particles ($PM_{1–10}$, −2.07±2.10‰), a trend consistent with previous findings (Chen, T. Y. et al., 2022). This size-dependent distribution likely reflects isotopic fractionation occurring during HNO_3 formation and its subsequent partitioning across different size modes. In environments (nearby coast) proximal to major NO_x sources, HNO_3 may react preferentially with coarse-mode particles (e.g., NaCl or mineral dust), forming $\delta^{15}N$-enriched pNO_3^-. The residual NO_x pool, consequently depleted in $\delta^{15}N$, subsequently forms HNO_3 that condenses onto fine-mode particles as they undergo transport toward the sampling site (Gobel et al., 2013). However, it is important to note that the complex physical and chemical dynamic processes within the air parcel during its transit, as detailed above, may diminish these distinct isotopic signatures under varying daily meteorological conditions.

3.4.2. Using $\delta^{18}O\text{-}NO_3^-$ to estimate contributions of pNO_3^- formation pathways

The daily concentration-weighted $\delta^{18}O\text{-}NO_3^-$ ranged from 30.98 to 73.27‰, with an average value of 51.82±16.47‰ (Fig. 2h). Similar to $\delta^{15}N\text{-}NO_3^-$, these values align with measurements from other mountain regions such as 10.8−92.4‰ at Mt. Lulin (Guha et al., 2017) and 64.71±11.52‰ at the Himalayan-Tibetan Plateau (Lin et al., 2021), but are lower than previous winter observations (72.66±3.42‰) (Chen, T. Y. et al., 2022), as illustrated in Fig. S11. In contrast, $\delta^{18}O\text{-}NO_3^-$ at urban sites such as Changchun (68.16±9.52‰) and Beijing (83.8±13.4‰) are substantially higher, consistent with O_3-dominated oxidation under polluted conditions. The relatively lower $\delta^{18}O\text{-}NO_3^-$ values at Xitou and other mountain sites suggest that RO_2-initiated pathways contribute more substantially to nitrate formation under less-polluted conditions. A sharp decrease in $\delta^{18}O\text{-}NO_3^-$ from 70.44‰ (18D) to 33.81‰ (18N and 19D) occurred during the fog, coinciding with $\delta^{15}N\text{-}NO_3^-$ depletion. This shift from O_3- to RO_2-dominated oxidation, is likely driven by stagnant winds, suppressed urban input, and enhanced local aqueous-phase chemistry under high RH.

Notably, no significant systematic size-dependent trend of $\delta^{18}O\text{-}NO_3^-$ on particle size was observed (Fig. 6b). The spatial heterogeneity of oxidants (O_3 and RO_2), coupled with the complex HNO_3 partitioning dynamics within the air parcel, likely erases any size-dependent isotopic pattern and daily variation. However, the $\delta^{15}N\text{-}NO_3^-$ vs. $\delta^{18}O\text{-}NO_3^-$ relationship (Fig. 6c, S12, and S13) resolves two geochemically distinct regimes reflecting contrasting formation environments and aerosol histories. The higher $\delta^{18}O\text{-}NO_3^-$ (55−83‰) with enriched $\delta^{15}N\text{-}NO_3^-$ (−6 to 1‰) can be assigned as an urban/transported regime. Freshly emitted in metropolitan areas contributed to elevated $\delta^{15}N$, while O_3-driven oxidation leads to high $\delta^{18}O$ (Gobel et al., 2013). The observed lower $\delta^{18}O\text{-}NO_3^-$ (9−38‰) and depleted $\delta^{15}N\text{-}NO_3^-$ (−10 to −2‰) is assigned as a rural/fog regime. These signatures reflect RO_2-initiated oxidation and $\delta^{15}N$-depleted NO_x from locally derived biogenic precursors or after extensive fractionation during transport, particularly under stagnant conditions. A moderate positive correlation ($r = 0.66$) between $\delta^{18}O\text{-}NO_3^-$ and $\delta^{15}N\text{-}NO_3^-$ further highlights the intrinsic interplay between oxidation processes and nitrogen cycling at the site. These data demonstrate a $\delta^{18}O\text{-}NO_3^-$ and $\delta^{15}N\text{-}NO_3^-$ relationship that covers a broad isotopic range, spanning from the signatures observed at the Himalayan-Tibetan Plateau to those at regional background sites like Mt. Lulin (Fig. S14).

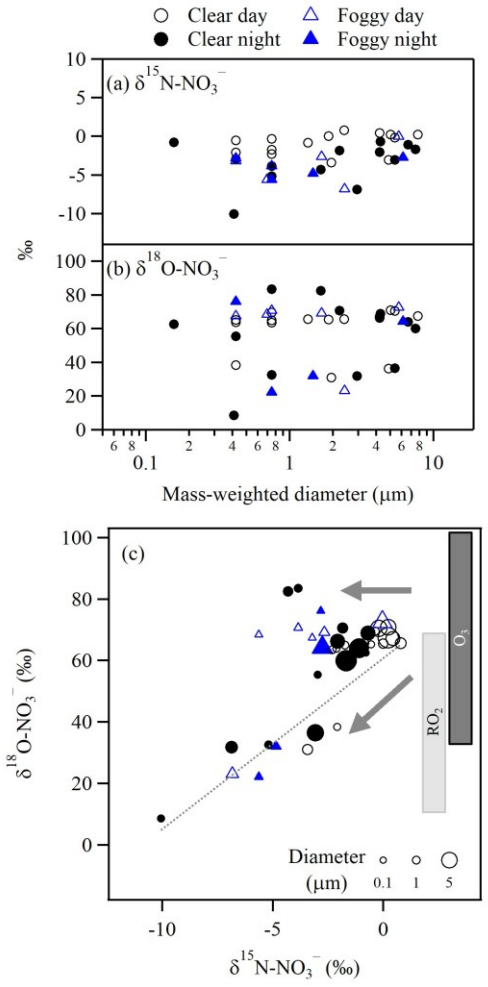

Figure 6. Size-resolved isotopic composition of pNO_3^-. (a) $\delta^{15}N\text{-}NO_3^-$ values as a function of mass-weighted particle diameter. (b) $\delta^{18}O\text{-}NO_3^-$ values as a function of mass-weighted particle diameter. (c) Two-dimensional plot of $\delta^{15}N$ versus $\delta^{18}O$ across particle sizes. The dotted line provides a visual guide to possible source groupings. The gray boxes labeled "RO_2" and "O_3" indicate the potential $\delta^{18}O\text{-}NO_3^-$ ranges resulting from reactions with RO_2 and O_3, respectively.

Formation pathways of pNO_3^- were quantitatively analyzed using the MixSIAR framework based on $\delta^{18}O\text{-}NO_3^-$ values, as shown in Fig. 7. During daytime periods characterized by low $\delta^{18}O\text{-}NO_3^-$ values (31−41‰) and low CO concentrations (< 0.22ppm, 17D, 19D, and 23D), $P_{RO_2\text{-}OH1}$ accounted for 82−92% of pNO_3^- formation (Figs. 7a and 7b). These conditions are consistent with periods with limited influence from urban air masses, suggesting the dominance of local RO_2 oxidation processes. In contrast, during daytime with higher $\delta^{18}O\text{-}NO_3^-$ values (63−70‰) and to elevated CO concentrations (0.24−0.27 ppm, 18D, 21D, 22D), the dominant pathways shifted toward $P_{RO_2\text{-}OH2}$, $P_{O_3\text{-}OH1}$, and $P_{O_3\text{-}OH2}$, contributing an average of 29±1%, 27±3%, and 28±5%, respectively. This shift could probably reflect the enhanced transport of urban air masses enriched in O_3 and NO_x precursors.

Although nighttime nitrate formation is theoretically dominated by heterogeneous reactions, our results reveal a more complex process. On nights with elevated $\delta^{18}O\text{-}NO_3^-$ values, heterogeneous pathways ($P_{RO_2\text{-}het}$ and $P_{O_3\text{-}het}$) were the dominant contributors, accounting for 33±6% and 47±9% of pNO_3^- formation on 19N, 21N, 23N. In contrast, on nights with lower $\delta^{18}O\text{-}NO_3^-$ values (32−43‰, 17N, 18N, 20N, and 22N), $P_{RO_2\text{-}OH1}$ remained a major contributor, accounting for 80−94% of formation. This high $P_{RO_2\text{-}OH1}$ might stem from the residual pNO_3^- from daytime, or nighttime ·OH generated via reactions between O_3 and alkenes/terpenes (Kroll et al., 2001; Aschmann et al., 2002). The weak night-to-night covariation between $\delta^{18}O\text{-}NO_3^-$ and CO concentrations further suggests that nighttime nitrate isotope signatures are governed by the interplay among fog processing, reduced advection, and heterogeneous chemistry, rather than transport intensity alone.

A distinct shift in nitrate formation pathways was observed during the fog. On 18D, high $\delta^{18}O\text{-}NO_3^-$ values (70‰) and elevated CO concentrations (0.24 ppm) were associated with the dominance of $P_{RO_2\text{-}OH2}$ (30±20%) and $P_{O_3\text{-}OH2}$ (36±16%), indicating that O_3 from transported urban precursors remained active (Fig. S15). As fog intensified during 18N and persisted into 19D, $\delta^{18}O\text{-}NO_3^-$ values decreased sharply to ~34‰, and $P_{RO_2\text{-}OH1}$ became dominant (93±5% on 18N, and 90±5% on 19D). This transition is driven by two coupled effects: (1) the attenuation of incoming solar radiation suppresses O_3 photolysis and thereby reduces the availability of high-$\delta^{18}O$ oxidants, and (2) the scavenging of long-range transport by wet deposition diminishes the influx of urban NO_x and O_3. Together, these foggy conditions favor locally derived low-$\delta^{18}O$ RO_2 cycling as the predominant oxidant driving nitrate formation.

Distinguishing the relative contributions helps clarify how nitrate formation processes vary with air mass origin, photochemical activity, and fog processing, which is directly relevant to emission control strategies since the efficacy of nitrate reduction depends on the dominant oxidation pathway. At the global scale, model estimated that the NO_2 + ·OH (same as our $P_{O_3\text{-}OH1}/P_{O_3\text{-}OH2}$) and N_2O_5 hydrolysis (same as our $P_{RO_2\text{-}het}/P_{O_3\text{-}het}$) pathways each contributed approximately 41% to tropospheric nitrate formation (Alexander et al., 2020), while observation studies in both urban and mountain environments suggest that heterogeneous pathways become more important for nitrate formation under elevated pollution levels (Fan et al., 2020; Lin et al., 2021). The pathway apportionment presented here provides finer resolution than bulk gas-phase/heterogeneous partitioning by explicitly distinguishing RO_2- from O_3-initiated formation, which can be useful in regions where RO_2 oxidation dominates. However, given the limited number of sampling days in this campaign, the relationship between nitrate formation pathways and pollution intensity warrants further investigation across seasons and contrasting meteorological conditions.

Beyond inorganic HNO_3 formation, the total particulate nitrogen budget includes particulate organic nitrate (*p*ON) species, which can account for 17−31% of total particulate nitrogen (Yu et al., 2024) in mixed urban-biogenic environments, and up to 50% observed in urban plumes (Murphy et al., 2025). *p*ON forms via the reaction of NO with RO_2 ($NO + RO_2 \rightarrow RONO_2$) during the day, and NO_3 with alkenes and biogenic VOC at night ($NO_3 + R \rightarrow RONO_2$) (Murphy et al., 2025; Ward et al., 2025; Guo et al., 2024). These mechanisms operate through the same RO_2- and NO_3-driven pathways identified here ($P_{RO_2\text{-}OH1}$ / $P_{RO_2\text{-}OH2}$ and $P_{RO_2\text{-}het}/P_{O_3\text{-}het}$, respectively), suggesting that the oxidation chemistry inferred from $\delta^{18}O\text{-}NO_3^-$ signatures at Xitou also drives concurrent *p*ON production. Because isotope analysis in this study assumes TN comprises only NO_3^- and NH_4^+, organic nitrogen contribution

could bias the derived δ^{15}N-NH_4^+ toward the signature of *p*ON. While this was partially mitigated by excluding samples with low [NH_4^+] (<60% of ([TN]−[NN])), future research should prioritize direct δ^{15}N-NH_4^+ measurement, which would enable the estimation of organic nitrate isotopes via residual mass balance (i.e., [ON] = [TN] – [NH_4^+] – [NO_3^-]) and provide a more complete characterization of the Nr budget in mountain forest environments.

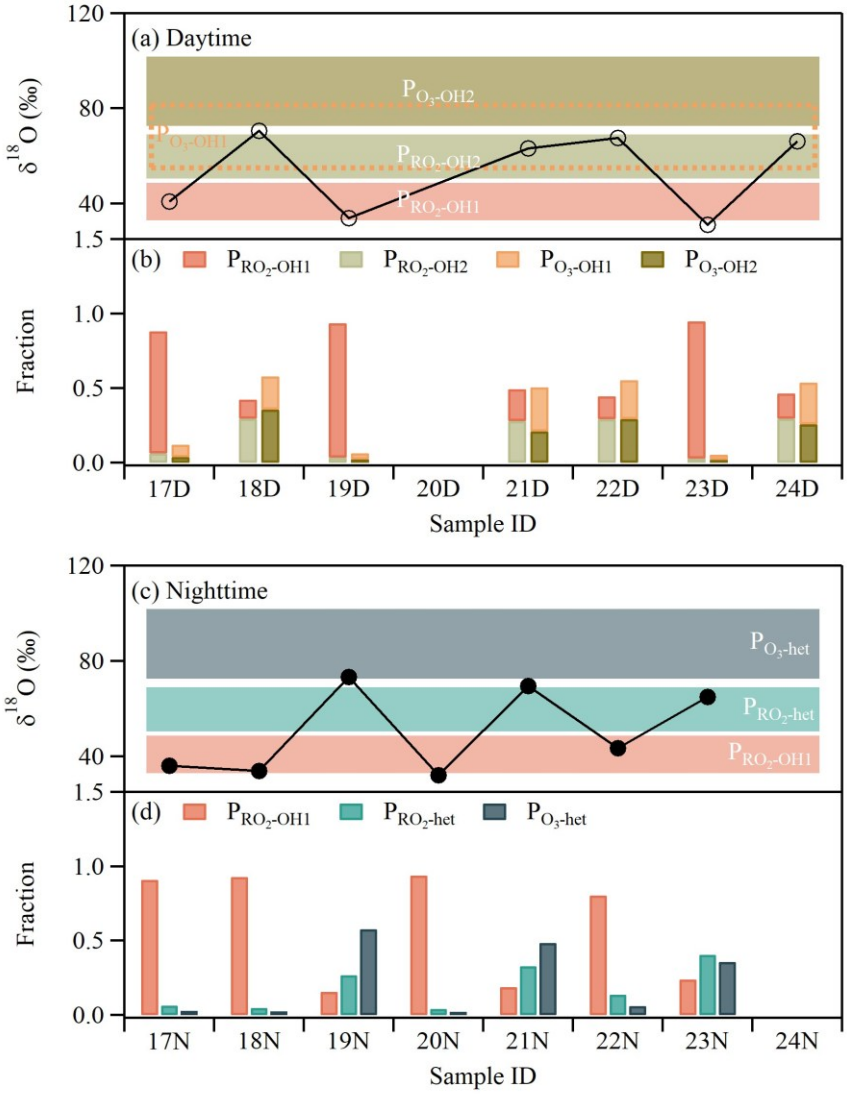

Figure 7. Contributions of nitrate formation pathways estimated by MixSIAR. (a, c) Measured δ^{18}O-NO_3^- values with the corresponding δ^{18}O ranges of potential formation pathways. (b, d) estimated fractional contributions of these pathways.

4. Conclusions

Our observations in a subtropical mountain forest in Taiwan revealed evident diurnal and meteorological influences on the transport and transformation of reactive nitrogen (Nr). Daytime particle concentrations consistently exceeded nighttime levels, reflecting upslope transport of urban plumes, while a 26-hour fog event suppressed urban input and enhanced local transformation processes. During the prolonged fog, progressive decreases in δ^{15}N-NH_4^+ and δ^{15}N-NO_3^- values indicated sustained isotopic depletion on the particle phase due to partitioning of species from the isotopically depleted gas phase, combining with the preferential wet depletion of the

earlier-formed δ^{15}N-enriched particles under stagnant conditions. Simultaneously, δ^{18}O-NO_3^- values shifted markedly, suggesting a transition from O_3- to RO_2-dominated pNO_3^- formation pathways. Unlike previous studies of shorter fog episodes, this extended fog allowed more precise identification of isotopic fractionation dynamics and nitrate evolution pathways.

Under clear conditions, size-resolved δ^{15}N-NH_4^+ exhibited a bell-shaped distribution, peaking at ~15‰ in the accumulation mode (~0.5–2 μm) and decreasing to ~7‰ in both the ultrafine and coarse fractions. This pattern reflects a transition between local isotopically light NH_3 and conservative transport of combustion-derived, sulfate-bound NH_4^+ from urban source regions. During fog, this size-dependent gradient flattened as weakened winds suppressed advection and enhanced aqueous-phase re-equilibration across all size bins. Concurrently, size-resolved δ^{15}N-NO_3^- and δ^{18}O-NO_3^- patterns further revealed two distinct pNO_3^- formation regimes: one associated with transport from urban plumes under O_3 oxidation, and another linked to local RO_2-driven processes with greater isotopic depletion and biogenic contributions.

Bayesian source apportionment based on δ^{15}N-NH_3^0 constraints indicates that combustion-related emissions contributed 50–83% of total NH_3, a finding that remained robust (88–95% in sensitivity tests) across varying meteorological conditions. This persistent anthropogenic signature highlights the resilience of combustion sources in shaping local nitrogen budgets and underscores the potential for regional emission control strategies targeting anthropogenic NH_3, which represent a highly efficient mitigation for $PM_{2.5}$ reduction in Taiwan. Furthermore, isotopic analysis of δ^{18}O-NO_3^- revealed that RO_2-initiated oxidation accounted for 42–95% of daytime pNO_3^- formation and remained substantial at night, with heterogeneous reactions accounting for 6–84%. These findings highlight the significance of RO_2 chemistry in nitrate formation, particularly in forested, high-humidity environments where biogenic VOC emissions promote RO_2 radical production.

Despite these insights, certain methodological uncertainties remain. Estimation of δ^{15}N-NH_3 from particulate δ^{15}N-NH_4^+ relied on simplified equilibrium fractionation assumptions that may underestimate kinetic effects, potentially biasing source attribution toward combustion-related NH_3 sources. Furthermore, overlapping isotopic signatures complicate the isolation of individual NO_x to pNO_3^- oxidation pathways. As these conclusions reflect processes observed during a one-week spring campaign, expanded measurements across multiple seasons and meteorological regimes would be needed to establish climatological representativeness. Future studies should integrate direct gas-phase isotope observations, chamber studies of aqueous-phase reactions, and region-specific source inventories to refine isotopic models. Such advancements will improve the differentiation between urban and biogenic contributions, thereby enabling a more rigorous evaluation of the effectiveness of targeted emission reduction strategies.

Code availability. Codes are available upon request.

Data availability. Data are available upon request.

Sample availability. Samples are no longer available due to full consumption during analytical procedures.

Author contribution.

WCL: data curation, formal analysis, MixSIAR analysis, visualization, writing original draft; **MHH:** laboratory experiments, data curation, formal analysis; **WCH:** field observations, filter sample collection, laboratory experiments, data curation; **JPC:** CMAQ modeling and analysis; **YJL:** meteorological data collection; **HR:** supervision of isotope measurements and analysis; **HMH:** project design, project supervision, data discussion, manuscript review and editing. All authors approved the final version of the manuscript.

Competing interests. The authors declare that they have no conflict of interest.

Disclaimer. Copernicus Publications remains neutral with regard to jurisdictional claims in published maps and institutional affiliations.

Acknowledgments. The authors acknowledge Hsu-Hung Lee and Ting-Yu Chen for their assistance with field observations, filter sampling, and preliminary data analysis. We also thank Prof. Jr-Chuan Huang from the Department of Geography, National Taiwan University, for IC instrumentation support, and the administration of the Xitou Experimental Forest, College of Bio-Resources and Agriculture, National Taiwan University, for local site support. AI tools (ChatGPT, Gemini, and Claude) were used to improve the clarity of language; all scientific content was developed and verified by the authors.

Financial support. This study was supported by the National Science and Technology Council of Taiwan (Grant Nos. 112-2111-M-002-014, 113-2111-M-002-012, and 114-2111-M-002-014). W.-C. Lee received support from the National Science and Technology Council of Taiwan (Grant Nos. 113-2811-M-002-114 and 114-2811-M-002-083).

References

Alexander, B., Sherwen, T., Holmes, C. D., Fisher, J. A., Chen, Q., Evans, M. J., and Kasibhatla, P.: Global inorganic nitrate production mechanisms: comparison of a global model with nitrate isotope observations, Atmos. Chem. Phys., 20, 3859-3877, https://doi.org/10.5194/acp-20-3859-2020, 2020.

Aschmann, S. M., Arey, J., and Atkinson, R.: OH radical formation from the gas-phase reactions of O_3 with a series of terpenes, Atmos. Environ., 36, 4347-4355, https://doi.org/10.1016/S1352-2310(02)00355-2, 2002.

Böhlke, J. K., Mroczkowski, S. J., and Coplen, T. B.: Oxygen isotopes in nitrate: new reference materials for ^{18}O:^{17}O:^{16}O measurements and observations on nitrate-water equilibration, Rapid Commun. Mass Spectrom., 17, 1835-1846, https://doi.org/10.1002/rcm.1123, 2003.

Chang, Y., Zhang, Y., Wang, Q., Shao, S., Bao, M., Zhang, C., and Lehmann, M. F.: Nitrogen isotope fractionation associated with ammonia gas-to-aerosol conversion and implications for determining isotopic source signatures and tracing atmospheric ammonium origins, Environ. Sci. Technol., 59, 22110-22121, https://doi.org/10.1021/acs.est.5c11271, 2025.

Chang, Y., Zhang, Y., Tian, C., Zhang, S., Ma, X., Cao, F., Liu, X., Zhang, W., Kuhn, T., and Lehmann, M. F.: Nitrogen isotope fractionation during gas-to-particle conversion of NO_x to NO_3^- in the atmosphere – implications for isotope-based NO_x source apportionment, Atmos. Chem. Phys., 18, 11647-11661, https://doi.org/10.5194/acp-18-11647-2018, 2018.

Chen, C.-L., Chen, T.-Y., Hung, H.-M., Tsai, P.-W., Chou, C. C. K., and Chen, W.-N.: The influence of upslope fog on hygroscopicity and chemical composition of aerosols at a forest site in Taiwan, Atmos. Environ., 246, 118150, https://doi.org/10.1016/j.atmosenv.2020.118150, 2021.

Chen, T. Y., Chen, C. L., Chen, Y. C., Chou, C. C. K., Ren, H., and Hung, H. M.: Source apportionment and evolution of N-containing aerosols at a rural cloud forest in Taiwan by isotope analysis, Atmos. Chem. Phys., 22, 13001-13012, https://doi.org/10.5194/acp-22-13001-2022, 2022.

Chen, Z.-L., Song, W., Hu, C.-C., Liu, X.-J., Chen, G.-Y., Walters, W. W., Michalski, G., Liu, C.-Q., Fowler, D., and Liu, X.-Y.: Significant contributions of combustion-related sources to ammonia emissions, Nat. Commun., 13, 7710, https://doi.org/10.1038/s41467-022-35381-4, 2022.

Dubey, M. K., Mohrschladt, R., Donahue, N. M., and Anderson, J. G.: Isotope specific kinetics of hydroxyl radical (OH) with water (H_2O): Testing models of reactivity and atmospheric fractionation, J. Phys. Chem. A, 101, 1494-1500, https://doi.org/10.1021/jp962332p, 1997.

Ervens, B.: Modeling the processing of aerosol and trace gases in clouds and fogs, Chem. Rev., 115, 4157-4198, https://doi.org/10.1021/cr5005887, 2015.

Fan, M.-Y., Zhang, Y.-L., Lin, Y.-C., Cao, F., Zhao, Z.-Y., Sun, Y., Qiu, Y., Fu, P., and Wang, Y.: Changes of emission sources to nitrate aerosols in Beijing after the clean air actions: Evidence from dual isotope compositions, J. Geophys. Res.: Atmos., 125, e2019JD031998, https://doi.org/10.1029/2019JD031998, 2020.

Freyer, H. D., Kley, D., Volz-Thomas, A., and Kobel, K.: On the interaction of isotopic exchange processes with photochemical reactions in atmospheric oxides of nitrogen, J. Geophys. Res.: Atmos., 98, 14791-14796, https://doi.org/10.1029/93JD00874, 1993.

Galloway, J. N., Townsend, A. R., Erisman, J. W., Bekunda, M., Cai, Z., Freney, J. R., Martinelli, L. A., Seitzinger, S. P., and Sutton, M. A.: Transformation of the nitrogen cycle: Recent trends, questions, and potential solutions, Science, 320, 889-892, https://doi.org/doi:10.1126/science.1136674, 2008.

Gobel, A. R., Altieri, K. E., Peters, A. J., Hastings, M. G., and Sigman, D. M.: Insights into anthropogenic nitrogen deposition to the North Atlantic investigated using the isotopic composition of aerosol and rainwater nitrate, Geophys. Res. Lett., 40, 5977-5982, https://doi.org/10.1002/2013GL058167, 2013.

Gong, C., Tian, H., Liao, H., Pan, N., Pan, S., Ito, A., Jain, A. K., Kou-Giesbrecht, S., Joos, F., Sun, Q., Shi, H., Vuichard, N., Zhu, Q., Peng, C., Maggi, F., Tang, F. H. M., and Zaehle, S.: Global net climate effects of anthropogenic reactive nitrogen, Nature, 632, 557-563, https://doi.org/10.1038/s41586-024-07714-4, 2024.

Guha, T., Lin, C. T., Bhattacharya, S. K., Mahajan, A. S., Ou-Yang, C.-F., Lan, Y.-P., Hsu, S. C., and Liang, M.-C.: Isotopic ratios of nitrate in aerosol samples from Mt. Lulin, a high-altitude station in Central Taiwan, Atmos. Environ., 154, 53-69, https://doi.org/10.1016/j.atmosenv.2017.01.036, 2017.

Guo, F., Bui, A. A. T., Schulze, B. C., Dai, Q., Yoon, S., Shrestha, S., Wallace, H. W., Sanchez, N. P., Alvarez, S., Erickson, M. H., Sheesley, R. J., Usenko, S., Flynn, J., and Griffin, R. J.: Airmass history, night-time particulate organonitrates, and meteorology impact urban SOA formation rate, Atmos. Environ., 322, 120362, https://doi.org/10.1016/j.atmosenv.2024.120362, 2024.

Haagen-Smit, A. J., Bradley, C. E., and Fox, M. M.: Ozone formation in photochemical oxidation of organic substances, Ind. Eng. Chem., 45, 2086-2089, https://doi.org/10.1021/ie50525a044, 1953.

Hall, S. J., Ogata, E. M., Weintraub, S. R., Baker, M. A., Ehleringer, J. R., Czimczik, C. I., and Bowling, D. R.: Convergence in nitrogen deposition and cryptic isotopic variation across urban and agricultural valleys in northern Utah, J. Geophys. Res.: Biogeosci., 121, 2340-2355, https://doi.org/10.1002/2016JG003354, 2016.

Hastings, M. G., Sigman, D. M., and Lipschultz, F.: Isotopic evidence for source changes of nitrate in rain at Bermuda, J. Geophys. Res.: Atmos., 108, 4790, https://doi.org/10.1029/2003JD003789, 2003.

Heaton, T. H. E., Spiro, B., and Robertson, S. M. C.: Potential canopy influences on the isotopic composition of nitrogen and sulphur in atmospheric deposition, Oecologia, 109, 600-607, https://doi.org/10.1007/s004420050122, 1997.

Holmes, R. M., Aminot, A., Kérouel, R., Hooker, B. A., and Peterson, B. J.: A simple and precise method for measuring ammonium in marine and freshwater ecosystems, Can. J. Fish. Aquat. Sci., 56, 1801-1808, https://doi.org/10.1139/f99-128, 1999.

Huang, P. C., Hung, H. M., Lai, H. C., and Chou, C. C. K.: Assessing the effectiveness of SO_2, NO_x, and NH_3 emission reductions in mitigating winter $PM_{2.5}$ in Taiwan using CMAQ, Atmos. Chem. Phys., 24, 10759-10772, https://doi.org/10.5194/acp-24-10759-2024, 2024.

Huang, W. C., Hung, H. M., Chu, C. W., Hwang, W. C., and Lung, S. C. C.: Deriving the hygroscopicity of ambient particles using low-cost optical particle counters, Atmos. Meas. Tech., 17, 6073-6084, https://doi.org/10.5194/amt-17-6073-2024, 2024.

Kawashima, H., Yoshida, O., and Suto, N.: Long-term source apportionment of ammonium in $PM_{2.5}$ at a suburban and a rural site using stable nitrogen isotopes, Environ. Sci. Technol., 57, 1268-1277, https://doi.org/10.1021/acs.est.2c06311, 2023.

Kroll, J. H., Clarke, J. S., Donahue, N. M., Anderson, J. G., and Demerjian, K. L.: Mechanism of HO_x formation in the gas-phase ozone−alkene reaction. 1. Direct, pressure-dependent measurements of prompt OH yields, J. Phys. Chem. A, 105, 1554-1560, https://doi.org/10.1021/jp002121r, 2001.

Kroopnick, P. and Craig, H.: Atmospheric oxygen: Isotopic composition and solubility fractionation, Science, 175, 54-55, https://doi.org/10.1126/science.175.4017.54, 1972.

Kundu, S., Kawamura, K., and Lee, M.: Seasonal variation of the concentrations of nitrogenous species and their nitrogen isotopic ratios in aerosols at Gosan, Jeju Island: Implications for atmospheric processing and source changes of aerosols, J. Geophys. Res.: Atmos., 115, D20305, https://doi.org/10.1029/2009JD013323, 2010.

Lin, Y.-C., Zhang, Y.-L., Yu, M., Fan, M.-Y., Xie, F., Zhang, W.-Q., Wu, G., Cong, Z., and Michalski, G.: Formation mechanisms and source apportionments of airborne nitrate aerosols at a Himalayan-Tibetan Plateau site: Insights from nitrogen and oxygen isotopic compositions, Environ. Sci. Technol., 55, 12261-12271, https://doi.org/10.1021/acs.est.1c03957, 2021.

Lin, Z., Ji, X., Xu, L., Chen, G., Yang, C., Zhang, K., Zhang, F., Li, L., Chen, Y., and Chen, J.: Enhanced NO_2-driven multiphase formation of particulate nitrate and sulfate under high-humidity conditions, npj Clim. Atmos. Sci., 9, 76, https://doi.org/10.1038/s41612-026-01352-5, 2026.

Meng, W., Zhong, Q., Yun, X., Zhu, X., Huang, T., Shen, H., Chen, Y., Chen, H., Zhou, F., Liu, J., Wang, X., Zeng, E. Y., and Tao, S.: Improvement of a global high-resolution ammonia emission inventory for combustion and industrial sources with new data from the residential and transportation sectors, Environ. Sci. Technol., 51, 2821-2829, https://doi.org/10.1021/acs.est.6b03694, 2017.

Moore, H.: The isotopic composition of ammonia, nitrogen dioxide and nitrate in the atmosphere, Atmos. Environ., 11, 1239-1243, https://doi.org/10.1016/0004-6981(77)90102-0, 1977.

Morin, S., Savarino, J., Frey, M. M., Domine, F., Jacobi, H.-W., Kaleschke, L., and Martins, J. M. F.: Comprehensive isotopic composition of atmospheric nitrate in the Atlantic Ocean boundary layer from 65°S to 79°N, J. Geophys. Res.: Atmos., 114, D05303, https://doi.org/10.1029/2008JD010696, 2009.

Murphy, S. E., Buenconsejo, R. S., Draper, D. C., Crounse, J. D., Baliaka, H. D., Ward, R. X., Schulze, B. C., Rezgui, S. P., Ball, K., Susskind, T., Kappaganthula, G., and Wennberg, P. O.: Multi-functional organic nitrogen in the Los Angeles Air Basin, ACS ES&T Air, 2, 2009-2027, https://doi.org/10.1021/acsestair.5c00206, 2025.

Pan, Y., Tian, S., Liu, D., Fang, Y., Zhu, X., Zhang, Q., Zheng, B., Michalski, G., and Wang, Y.: Fossil fuel combustion-related emissions dominate atmospheric ammonia sources during severe haze episodes: Evidence from ^{15}N-stable isotope in size-resolved aerosol ammonium, Environ. Sci. Technol., 50, 8049-8056, https://doi.org/10.1021/acs.est.6b00634, 2016.

Proemse, B. C., Mayer, B., Chow, J. C., and Watson, J. G.: Isotopic characterization of nitrate, ammonium and sulfate in stack $PM_{2.5}$ emissions in the Athabasca Oil Sands Region, Alberta, Canada, Atmos. Environ., 60, 555-563, https://doi.org/10.1016/j.atmosenv.2012.06.046, 2012.

Pye, H. O. T., Nenes, A., Alexander, B., Ault, A. P., Barth, M. C., Clegg, S. L., Collett Jr, J. L., Fahey, K. M., Hennigan, C. J., Herrmann, H., Kanakidou, M., Kelly, J. T., Ku, I. T., McNeill, V. F., Riemer, N., Schaefer, T., Shi, G., Tilgner, A., Walker, J. T., Wang, T., Weber, R., Xing, J., Zaveri, R. A., and Zuend, A.: The acidity of atmospheric particles and clouds, Atmos. Chem. Phys., 20, 4809-4888, https://doi.org/10.5194/acp-20-4809-2020, 2020.

Romer, P. S., Duffey, K. C., Wooldridge, P. J., Allen, H. M., Ayres, B. R., Brown, S. S., Brune, W. H., Crounse, J. D., de Gouw, J., Draper, D. C., Feiner, P. A., Fry, J. L., Goldstein, A. H., Koss, A., Misztal, P. K., Nguyen, T. B., Olson, K., Teng, A. P., Wennberg, P. O., Wild, R. J., Zhang, L., and Cohen, R. C.: The lifetime of nitrogen oxides in an isoprene-dominated forest, Atmos. Chem. Phys., 16, 7623-7637, https://doi.org/10.5194/acp-16-7623-2016, 2016.

Savard, M. M., Cole, A., Smirnoff, A., and Vet, R.: $\delta^{15}N$ values of atmospheric N species simultaneously collected using sector-based samplers distant from sources – Isotopic inheritance and fractionation, Atmos. Environ., 162, 11-22, https://doi.org/10.1016/j.atmosenv.2017.05.010, 2017.

Stock, B. C. and Semmens, B. X.: MixSIAR GUI User Manual. Version 3.1, https://doi.org/10.5281/zenodo.1209993, 2016.

Stock, B. C., Jackson, A. L., Ward, E. J., Parnell, A. C., Phillips, D. L., and Semmens, B. X.: Analyzing mixing systems using a new generation of Bayesian tracer mixing models, PeerJ, 6, e5096, https://doi.org/10.7717/peerj.5096, 2018.

Ti, C., Gao, B., Luo, Y., Wang, X., Wang, S., and Yan, X.: Isotopic characterization of NH_x-N in deposition and major emission sources, Biogeochemistry, 138, 85-102, https://doi.org/10.1007/s10533-018-0432-3, 2018.

Tsai, I. C., Hsieh, P.-R., Hsu, H.-H., Tung, Y.-S., Chen, Y.-M., and Cheng, C.-T.: Climate change-induced impacts on $PM_{2.5}$ in Taiwan under 2 and 4 °C global warming, Atmos. Pollut. Res., 15, 102106, https://doi.org/10.1016/j.apr.2024.102106, 2024.

Vicars, W. C., Morin, S., Savarino, J., Wagner, N. L., Erbland, J., Vince, E., Martins, J. M. F., Lerner, B. M., Quinn, P. K., Coffman, D. J., Williams, E. J., and Brown, S. S.: Spatial and diurnal variability in reactive nitrogen oxide chemistry as reflected in the isotopic composition of atmospheric nitrate: Results from the CalNex 2010 field study, J. Geophys. Res.: Atmos., 118, 10,567-510,588, https://doi.org/10.1002/jgrd.50680, 2013.

Walters, W. W. and Michalski, G.: Theoretical calculation of oxygen equilibrium isotope fractionation factors involving various NO_y molecules, OH, and H_2O and its implications for isotope variations in atmospheric nitrate, Geochim. Cosmochim. Acta, 191, 89-101, https://doi.org/10.1016/j.gca.2016.06.039, 2016.

Walters, W. W., Karod, M., Willcocks, E., Baek, B. H., Blum, D. E., and Hastings, M. G.: Quantifying the importance of vehicle ammonia emissions in an urban area of northeastern USA utilizing nitrogen isotopes, Atmos. Chem. Phys., 22, 13431-13448, https://doi.org/10.5194/acp-22-13431-2022, 2022.

Walters, W. W., Song, L., Chai, J., Fang, Y., Colombi, N., and Hastings, M. G.: Characterizing the spatiotemporal nitrogen stable isotopic composition of ammonia in vehicle plumes, Atmos. Chem. Phys., 20, 11551-11567, https://doi.org/10.5194/acp-20-11551-2020, 2020.

Ward, R. X., Baliaka, H. D., Schulze, B. C., Kerr, G. H., Crounse, J. D., Hasheminassab, S., Bahreini, R., Dillner, A. M., Russell, A., Ng, N. L., Wennberg, P. O., Flagan, R. C., and Seinfeld, J. H.: Poorly quantified trends in ammonium nitrate remain critical to understand future urban aerosol control strategies, Science Advances, 11, eadt8957, https://doi.org/10.1126/sciadv.adt8957, 2025.

Weigand, M. A., Foriel, J., Barnett, B., Oleynik, S., and Sigman, D. M.: Updates to instrumentation and protocols for isotopic analysis of nitrate by the denitrifier method, Rapid Commun. Mass Spectrom., 30, 1365-1383, https://doi.org/10.1002/rcm.7570, 2016.

Wu, C., Cao, C., Li, J., Lv, S., Li, J., Liu, X., Zhang, S., Liu, S., Zhang, F., Meng, J., and Wang, G.: Different physicochemical behaviors of nitrate and ammonium during transport: a case study on Mt. Hua, China, Atmos. Chem. Phys., 22, 15621-15635, https://doi.org/10.5194/acp-22-15621-2022, 2022.

Xu, W., Kuang, Y., Xu, W., Liu, L., Xu, H., Wang, X., Liu, Y., Cheng, H., Zhang, X., Zhai, M., Liu, C., Liang, L., Zhang, G., Luo, B., Tao, J., Liu, J., Zhao, H., Ren, S., Zhou, G., Liu, P., Xu, X., and Sun, Y.: Efficient nitrate formation in fog events implicates fog interstitial aerosols as significant drivers of atmospheric chemistry, Environ. Sci. Technol., 58, 22298-22311, https://doi.org/10.1021/acs.est.4c09078, 2024.

Yu, H.-R., Zhang, Y.-L., Cao, F., Zhao, Z.-Y., Fan, M.-Y., and Yang, X.-Y.: Fog event is possibly a source rather than a sink of atmospheric nitrate aerosols: Insights from isotopic measurements in Nanjing, China, Appl. Geochem., 155, 105721, https://doi.org/10.1016/j.apgeochem.2023.105721, 2023.

Yu, X., Li, Q., Liao, K., Li, Y., Wang, X., Zhou, Y., Liang, Y., and Yu, J. Z.: New measurements reveal a large contribution of nitrogenous molecules to ambient organic aerosol, npj Clim. Atmos. Sci., 7, 72, https://doi.org/10.1038/s41612-024-00620-6, 2024.

Zhang, G., Hu, X., Sun, W., Yang, Y., Guo, Z., Fu, Y., Wang, H., Zhou, S., Li, L., Tang, M., Shi, Z., Chen, D., Bi, X., and Wang, X.: A comprehensive study about the in-cloud processing of nitrate through coupled measurements of individual cloud residuals and cloud water, Atmos. Chem. Phys., 22, 9571-9582, https://doi.org/10.5194/acp-22-9571-2022, 2022.

Zhang, Q., Jiang, X., Tong, D., Davis, S. J., Zhao, H., Geng, G., Feng, T., Zheng, B., Lu, Z., Streets, D. G., Ni, R., Brauer, M., van Donkelaar, A., Martin, R. V., Huo, H., Liu, Z., Pan, D., Kan, H., Yan, Y., Lin, J., He, K., and Guan, D.: Transboundary health impacts of transported global air pollution and international trade, Nature, 543, 705-709, https://doi.org/10.1038/nature21712, 2017.

Zhou, W., Xu, W., Kim, H., Zhang, Q., Fu, P., Worsnop, D. R., and Sun, Y.: A review of aerosol chemistry in Asia: Insights from aerosol mass spectrometer measurements, Environ. Sci. Processes Impacts, 22, 1616-1653, https://doi.org/10.1039/D0EM00212G, 2020.

Supporting Information